18 (2026) 100262

Contents lists available at ScienceDirect

Superconductivity

journal homepage: www.sciencedirect.com/journal/superconductivity

Research Article

Correlated defect formation and pinning enhancement in 230 MeV Au-ion-irradiated superconducting Fe(Se,Te) thin films

Francesco Rizzo [a], Mario Scuderi [b,c,*], Valeria Braccini [d], Emilio Bellingeri [d], Michela Iebole [d], Alberto Martinelli [d], Nicola Manca [d], Matteo Cialone [d,e], Marina Putti [d,e], Andrea Augieri [a], Laura Piperno [a], Angelo Vannozzi [a], Maria Laura Amoruso [b,f], Fortunato Neri [f], Michela Fracasso [g,h], Roberto Gerbaldo [g,h], Gianluca Ghigo [g,h], Daniele Torsello [g,h], Laura Gozzelino [g,h,**]

[a] ENEA, Via E. Fermi 45, Frascati, 00044, Italy
[b] CNR–IMM, Strada VIII 5 Zona Industriale, Catania, 95121, Italy
[c] INFN-LNS, Via S. Sofia 62, Catania, 95123, Italy
[d] CNR – SPIN Genova, Corso Perrone 24, Genova, 16152, Italy
[e] Physics Department, University of Genova, Via Dodecaneso 33, Genova, 16146, Italy
[f] MIFT, University of Messina, Viale Ferdinando Stagno D'Alcontres, Messina, 98166, Italy
[g] Department of Applied Science and Technology, Politecnico di Torino, C. So Duca Degli Abruzzi 24, Torino, 10129, Italy
[h] INFN Sezione di Torino, V. P. Giuria 1, Torino, 10125, Italy

ARTICLE INFO

Keywords:
Iron-based superconductors
Fe(Se,Te) thin films
Critical current density
Flux pinning
Heavy-ion irradiation
YSZ buffered substrate

ABSTRACT

Intrinsic properties of Fe(Se,Te), such as the high value of the upper critical field as well as the weaker dependence of the critical current density (J_c) on the grain misalignment than in cuprate superconductors, make this compound a promising candidate for the fabrication of high-field superconducting magnets. On the other hand, irradiation was demonstrated to be a powerful tool for tuning the pinning properties in superconducting materials. In this paper, we investigate the effect of 230 MeV Au-ion irradiation on J_c and pinning force (F_p) of biaxially-oriented Fe(Se,Te) films grown on YSZ substrate buffered with a thin Zr-doped CeO_2 epitaxial layer. This structure is interesting as it can be considered a precursor template for Fe(Se,Te) coated conductors. The irradiation produces correlated defects, which - on transmission electron microscope analysis - appear as slightly meandering tracks composed of dislocation chains placed parallel to the *c*-axis of the crystal lattice. The J_c measurements as a function of the applied magnetic field evidence an improvement at low temperatures, with a maximum modulated in both position and height by the irradiation fluence. In the same range of temperature, the development of the irradiation tracks strongly reduces the anisotropy of the critical current density by varying the applied field orientation. Likewise, the F_p analysis highlights that irradiation defects behave as two-dimensional extended defects, which strengthen the point-pinning landscape active before irradiation. Conversely, approaching the transition temperature, the effectiveness of the irradiation-induced defects decreases and a widespread J_c and F_p worsening occurs.

1. Introduction

The numerous Iron-Based Superconductors (IBS) families are of considerable interest under several points of view, spanning from the study of their fundamental properties [1], to the strategies to increase the superconducting transition temperature and critical current density [2], to the technologies to fabricate long-length conductors which can be competitive in future high magnetic field applications such as nuclear fusion, energy devices, magnetic resonance imaging, and accelerator magnets, just to name a few [3], [4] [5].

The grain-boundary (GB) properties of IBSs are significantly more tolerant than those of cuprates: the suppression of the critical current, J_c,

* Corresponding author. CNR–IMM, Strada VIII 5 Zona Industriale, 95121, Catania, Italy.
** Corresponding author. Department of Applied Science and Technology, Politecnico di Torino, C. So Duca Degli Abruzzi 24, Torino, 10129, Italy
E-mail addresses: mario.scuderi@cnr.it (M. Scuderi), Laura.Gozzelino@polito.it (L. Gozzelino).

https://doi.org/10.1016/j.supcon.2026.100262
Received 8 March 2026; Received in revised form 14 May 2026; Accepted 14 May 2026
Available online 21 May 2026

at misoriented GBs is much weaker, and Fe(Se,Te) retains robust intergrain transport even for relatively large [001]-tilt misorientation angles [6] [7]. In addition, from an application perspective, IBS exhibit an upper critical field, H_{c2}, exceeding 50 T at low temperatures – even in the 11 family - which despite the critical temperature, T_c, lower than in cuprates, draw attention due to a very low H_{c2} anisotropy [8].

Exploiting these characteristics, efforts are underway to develop wires and tapes. The powder-in-tube (PIT) technique has been successful in fabricating conductors of the 122 family [4], [9], [10] [11] even in lengths up to 100 m [12], leading to the fabrication of a tesla-class coil [13]. The iron-chalcogenide 11 phase shows poor superconducting properties when fabricated in wires through PIT, due to the high reactivity of the phase with the metallic sheaths [14]. Instead, biaxially-oriented thin films can successfully be grown on different substrates: high J_c values are obtained in epitaxial films deposited on various single crystals [15], [16], [17] [18], buffered single crystals [19] [20], and commercial metallic templates produced by Ion-Beam-Assisted Deposition (IBAD) [21], [22] [23] or Rolling-Assisted Biaxially Textured Substrates (RABiTS) [19]' [24]. In particular, a significant advancement has recently been achieved when 1 m-long Fe(Se, Te)-Coated Conductors (CCs) were successfully grown by multiturn pulsed laser deposition on CeO_2-buffered IBAD MgO tape with a J_c over 2 MA/cm^2 at 4.2 K and self-field [3] and a single pancake coil using the Fe(Se,Te) coated conductor was subsequently fabricated [25].

Moreover, it has been shown that the RABiTS buffer layer architecture for the fabrication of 11 CCs can be much simpler than those developed for Rare-Earth Barium Copper Oxide (REBCO) CCs, thanks to the much lower growth temperatures (below 300 °C) and the absence of oxygen during the deposition: a single oxide layer [19] [20], [26], [27] [28] or TiN [29] is enough to reach the desired texturing and superconducting properties comparable to those of samples grown on single crystals. In particular, we extensively studied the deposition and epitaxial growth of Zr-doped CeO_2 (CZO) buffer layers for Fe(Se,Te) superconducting films both on Yttria-Stabilized Zirconia (YSZ) single crystals [30] and on NiW RABiTS substrates [31], finding that the CZO layers promote chemical matching with the buffer, mitigate the impact of buffer roughness, and protect the superconducting Fe(Se,Te) layer from oxygen contamination.

An efficient pinning landscape is a mandatory prerequisite to achieve large J_c with a controlled anisotropy. In such a context, ion irradiation is an excellent method to introduce controlled defect distributions inside a superconductor, allowing the creation of pinning centers with shape and density depending on the mass and energy of the particles and on their fluences, respectively [32] [33] In the case of high-energy heavy-ion irradiation, the dominant process in defect formation is ionization, i.e., the energy release by the impinging particles to the target electrons. This generates correlated defects distributed along the ion track that, when the energy loss exceeds a given threshold depending on the target material, can coalesce into continuous columnar tracks with a diameter of a few nanometers [34] [35].

In a previous paper [36], we already reported on the efficiency of columnar defects induced by 1.15 GeV Pb-ion irradiation in tuning the critical current density of $FeSe_{0.5}Te_{0.5}$ films grown on a CaF_2 crystalline substrate. On the other hand, it was proved that a few hundred MeV Au-ions, which can produce columnar tracks in cuprate superconductors, in IBSs only induce discontinuous tracks [37] with a metallic core [38]. Based on these outcomes, in this paper we investigated the effect of 230 MeV Au-ion irradiation on the pinning properties of Fe(Se,Te) films grown on CZO-buffered YSZ substrates. In this context, our goal was to assess whether irradiation-driven defects produced at these intermediate ion energies can act as an effective source of correlated pinning in Fe (Se,Te), and how they modify the balance between point-like and extended pinning contributions already present in the as-grown films. To this end, we combined a structural analysis capable of identifying the nature and spatial distribution of the irradiation-induced defects with a systematic investigation of the temperature, field, and angular dependence of the critical current density. This integrated approach enabled us to clarify how Au-ion irradiation reshapes the pinning landscape of Fe(Se,Te) and to determine under which operating conditions it provides an actual benefit for coated-conductor-relevant architectures.

The paper is organized as follows: in Section 2 we describe the sample preparation, irradiation procedure, and characterization techniques. In Section 3.1, the structural analysis is reported, with STEM imaging revealing the nature and morphology of irradiation-induced defects. In Section 3.2 the transport properties are discussed, including the J_c dependence on temperature and magnetic field, the evolution of pinning mechanisms analyzed through the Dew-Hughes model, and the angular anisotropy behavior. Finally, in Section 4, the main findings are summarized and conclusions are drawn.

2. Experimental details

CZO buffer layers were deposited via Metal Organic Decomposition on YSZ single crystal substrates as in [20]' [30]' [31]' [39]. The precursor solution was prepared dissolving stoichiometric amounts of Ce (III) acetate hydrate (Sigma Aldrich, 99.5%) and 5 mol.% Zr (IV) acetylacetonate (Sigma Aldrich, 98%) in propionic acid (Sigma Aldrich, 99.5%). Rotary evaporation was used to remove water and the excess of solvent until a concentration [Ce] = 0.3 M is reached. Then, the solution was deposited on 7.5 mm × 7.5 mm (100) YSZ single crystal substrate (MaTecK) by spin coating at 2000 rpm for 60 s and dried for 5 min at 120 °C in air. The as-obtained CZO films were pyrolyzed in air for 30 min at 450 °C and then crystallized for 30 min at 950 °C in 0.5 l/min Ar-5% H_2. Film final thickness was about 20 nm.

Fe(Se,Te) films were deposited on CZO buffered YSZ substrates by pulsed laser deposition in an ultra-high vacuum chamber (residual gas pressure during deposition of about 10^{-8} mbar) equipped with a Nd: YAG laser at 1064 nm and using a polycrystalline target with the nominal composition $FeSe_{0.5}Te_{0.5}$ synthesized using a two-step method [40]. First, a non-superconducting seed layer of about 35 nm was deposited at 400 °C at high laser repetition rate (10 Hz); then, the sample was cooled down to 200 °C for 110 nm top-layer deposition at 3 Hz. The films were deposited keeping the following parameters: a 2 J cm^{-2} laser fluence (2 mm^2 spot size) and a 5 cm distance between target and sample. The use of the seed layer was shown to be necessary to optimize the film properties [20].

One of the as-obtained films was patterned in two strips - each of them containing a 1-mm-long microbridge with a nominal width of 50 μm - by conventional UV lithography followed by water-cooled argon ion milling (Ar energy was 500 eV), as shown in Fig. 1(a). After the milling process, the sample was cleaned by mild sonication in acetone for a few tens of seconds and dried in nitrogen flow [41]. Finally, gold contacts were deposited on the sputtered current/voltage pads to improve the electrical signal-to-noise ratio.

One of the two strips was then irradiated at room temperature with 230 MeV Au ions at the Tandem accelerator of INFN - Legnaro National Laboratories (Italy). The same strip underwent two subsequent irradiations. Both the irradiations were performed in vacuum with the ion beam oriented perpendicular to the film surface, i.e. parallel to the *c*-axis of the Fe(Se,Te) crystal lattice. In both cases, only the bridge area was exposed to the beam (i.e., the region inside the red box in Fig. 1(b)), while current and voltage pads as well as the second strips were shielded by covering them with a thick and suitably shaped steel mask. The first irradiation fluence was $\phi = 2.90 \times 10^{11}$ cm^{-2}, corresponding to a fluence-equivalent field $B_\phi = 6$ T (B_ϕ is the magnetic field for which the flux-lines density in the sample is nominally equivalent to the surface density of impinging ions). After being characterized, the bridge was re-irradiated up to a total fluence of $\phi = 4.84 \times 10^{11}$ cm^{-2} (i.e., up to a fluence equivalent field $B_\phi = 10$ T). The ions were expected to mainly produce anisotropic correlated defects along the beam direction due to their inelastic scattering against the target atom electrons (ionization),

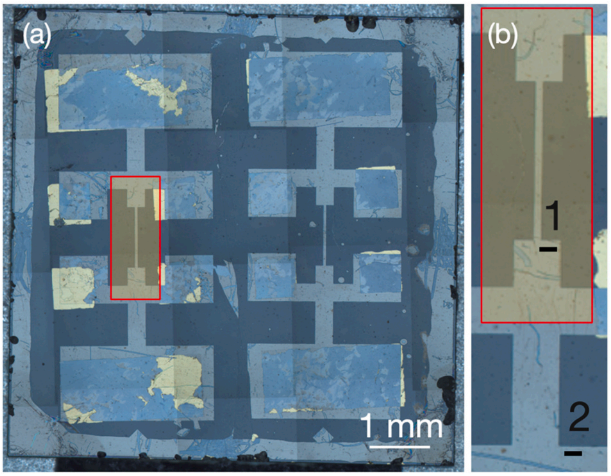

Fig. 1. (a) Optical image of the patterned sample featuring two strips, each of them containing a 1-mm-long microbridge. The left-side microbridge was irradiated with Au ions (red rectangle). (b) Enlarged view of the irradiated microbridge showing the extraction regions for the two TEM lamellae: irradiated (1) and non-irradiated (2).

encircled by a cloud of point-like defects due to secondary collisions [37]. Based on calculations performed with the Monte Carlo SRIM code [42], after crossing the Fe(Se,Te) film and the CZO buffer layer, the ions implanted into the YSZ substrate at a depth of about 12.6 μm. The computed profile of the implanted ions as well as the distribution of the energy released by inelastic scattering are plotted in Fig. 2.

For STEM characterization, two cross-sectional lamellae were prepared from selected areas of the irradiated strip using focused ion beam (FIB) milling. High-angle annular dark field (HAADF) and medium-angle annular dark field (MAADF) STEM imaging modes were employed to probe mass-thickness contrast and strain-related contrast, respectively. Prior to MAADF imaging, a systematic high-resolution Z-contrast STEM survey was conducted across multiple regions of the film to establish a reliable correspondence between contrast features and their structural origin (Fig. S1 and Fig. S2). MAADF imaging was then selected to map the spatial distribution of defects over the full film thickness within a single field of view at a magnification suitable to

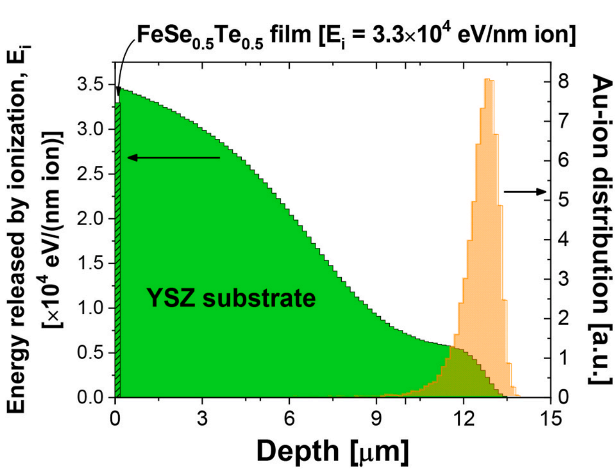

Fig. 2. Profile of the energy released by ionization (i.e. by Au-ion inelastic scattering against the target atom electrons) in both the Fe(Se,Te) film (thickness not to scale) and YSZ substrate and implantation profile of the Au-ions in the substrate. All the calculations were carried out by means of the Monte Carlo SRIM code. The presence of the buffer layer was always taken into account even though its contribution is negligible (and not shown in the picture) due to its small thickness. The zero depth corresponds to the sample surface.

encompass the entire film cross-section. This dual imaging strategy enabled a comprehensive analysis of structural features across the film. Additional SEM, XRD and SAED analyses were carried out to assess the macroscopic morphology, phase composition, and crystallographic orientation of the films. The corresponding results are reported in the Supporting Information (Fig. S5–S8).

To measure the transport properties as a function of temperature and applied field, the film was mounted in a cryogen-free cryostat, equipped with an 18 T superconducting magnet. A rotating probe was used to measure the J_c angular behavior, while keeping the current normal to the field direction (maximum Lorentz force configuration). All the measurements were performed using a four-point probe configuration with the standard 1 μV cm^{-1} electric field criterion.

3. Experimental results and discussion

3.1. Structural analysis

The optical micrograph in Fig. 1(a) shows the Fe(Se,Te) film patterned with the two strips. The irradiated strip was used to extract the cross-sectional lamellae. The enlarged view in Fig. 1(b) clearly indicates the extraction regions for the two lamellae: one from the irradiated zone (highlighted by a red rectangle, also in Fig. 1(a)) and the other from the non-irradiated zone.

The cross-sectional Z-contrast STEM image of the non-irradiated sample shown in Fig. 3(a) revealed a layered structure consisting of the YSZ substrate, the CZO buffer layer, and both the non-superconducting seed layer and the superconducting top layer of the Fe(Se,Te) film. Vertical contrast modulations across the Fe(Se,Te) film and the substrate, likely related to strain fields caused by lattice mismatch, are evident. The buffer layer exhibits notable roughness typical of the deposition method used, as previously documented [43], with an average thickness of approximately 20 nm. The seed and top layers of the Fe(Se,Te) film are approximately 35 nm and 110 nm thick, respectively, yielding a total thickness of around 165 nm including the buffer. Previous composition-sensitive studies on this system demonstrated that the seed layer tends to have a lower tellurium (Te) content compared to the top layer [20]. This compositional gradient is the result of differences in the growth conditions during the two-step deposition process and influences the superconducting behavior, with superconducting properties observed only in the top layer. The macroscopic morphology and phase purity of the films were further verified by complementary SEM and XRD analyses (see Supporting Information, Figs. S5 and S7), confirming the homogeneous structure of the film and the absence of detectable secondary phases.

Complementary MAADF-STEM imaging of the same region uncovers a wealth of structural details (Fig. 3(b), (c)). The contrast variations indicate deformed domains within the crystalline film. Here, "deformed" encompasses both strain-induced lattice distortions and crystallographic rotations/tilts that modify local diffraction conditions. The indicated domains show altered contrast due to changes in their structural orientation and/or elastic state relative to the surrounding matrix. In addition to these extended deformed regions, the image also exhibits localized bright spots with altered contrast, which can be attributed to point defects that induce local lattice distortions in their immediate vicinity. A representative example of such a feature, imaged at atomic resolution by high-resolution Z-contrast STEM, is shown in Fig. S2 of the Supporting Information, where the loss of crystalline coherence in a localized region of approximately 1 nm is directly visible. These point-like features represented individual defects or defect clusters that create highly localized strain fields, resulting in enhanced scattering contrast in MAADF imaging. Furthermore, linear contrast features are visible that correspond to GBs, where the strain fields generated at the interface between different grains create altered diffraction conditions. High-resolution Z-contrast imaging of such regions confirms the presence of adjacent grains with crystallographic

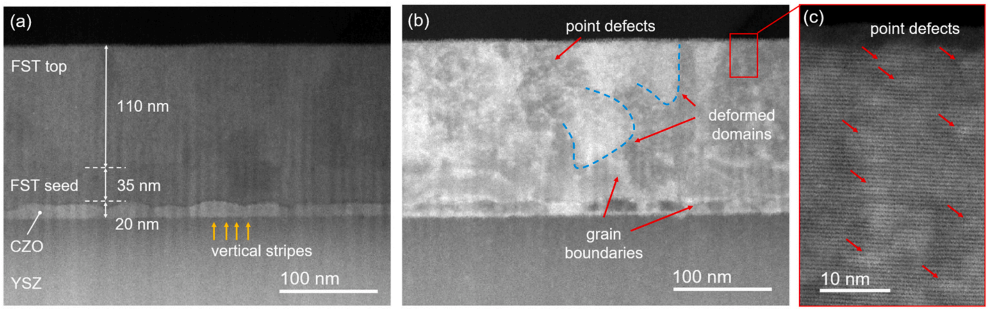

Fig. 3. (a) Cross-sectional Z-contrast STEM image of the as-grown Fe(Se,Te) film structure. Layers include: YSZ substrate, CZO buffer, Fe(Se,Te) seed, and Fe(Se,Te) top layer. Strain fields caused by lattice mismatch across the various layers are visible as vertical modulations (yellow arrows). (b) MAADF image of the same region, revealing deformed domains, GBs, and point defects throughout the film (red arrows). Contrast variations reflect local changes in diffraction conditions due to strain fields and crystallographic rotations. (c) Higher magnification detail of the boxed region in (b), showing point defects in the Fe(Se,Te) film.

misorientation, as shown in Fig. S1 of the Supporting Information. These three types of contrast variations - deformed domains, point defects, and GBs - collectively demonstrate the complex microstructural landscape accessible through MAADF imaging.

In the irradiated sample, structural deformations are significantly more pronounced. STEM imaging revealed surface and interfacial protrusions as reported in literature for similar iron-irradiated systems [36], particularly at the Fe(Se,Te)/CZO boundary and at the Fe(Se,Te) surface (Fig. 4(a)). A direct comparison between the as-grown and irradiated film surface morphology, highlighting the appearance of these nanoscale surface features, is reported in the Supporting Information (Fig. S6). These protrusions can be attributed to ion impact, especially at the interfaces where abrupt changes in density and mechanical properties occur. Furthermore, vertically extended defect tracks are observed running from the surface deep into the film (Fig. 4(b)). These tracks, originating near the surface protrusions, follow a slightly meandering path, oscillating around a central axis. In fact, such paths are not perfectly linear but instead trace a zigzagging progression probably caused by sequential elastic collisions of the Au-ions against the target atom nuclei and secondary collisions that come with it. These tracks are composed of dislocation chains, which are clearly resolved in the high-magnification view of Fig. 4(c).

A closer inspection of one of these tracks revealed that dislocations follow a staggered alignment, delineating the track's profile. Despite these structural disruptions, the crystalline nature of the film is largely preserved. The overall defect configuration introduced by the ion irradiation therefore consists of vertically oriented dislocation arrays, which can be interpreted as planar defects tracing the path of the ion through the film. Additional selected area electron diffraction analysis (Supporting Information, Fig. S8) reveals a splitting of the diffraction spots in the irradiated sample, indicating the presence of locally misoriented domains consistent with the defect structure observed by STEM.

3.2. *Transport properties*

The critical current density of the strips was measured in the temperature (T) range of 4.2 – 10 K as a function of the magnetic field, applied parallel to the film's c-axis, up to the maximum intensity of 18 T. Measurements were performed on both the pristine and irradiated strips. The latter was characterized after the first irradiation at $B_\phi = 6$ T and after the second one when a cumulative fluence-equivalent field $B_\phi = 10$ T was reached. The results are shown in Fig. 5.

At low temperatures, the self-field J_c values of the irradiated strip

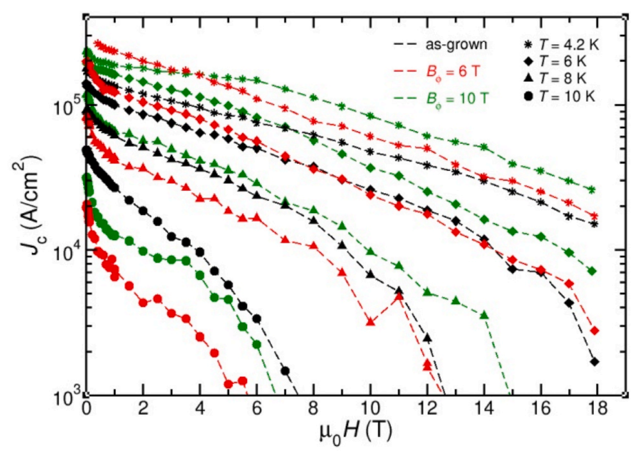

Fig. 5. In-field behavior, up to 18 T, of J_c for the investigated strips at different temperatures in the range 4.2 – 10 K (see symbol legend). J_c curves achieved on the as-grown strip are plotted in black, while the red and green curves refer to J_c values obtained on the irradiated strip at the dose equivalent fields, $B_\phi = 6$ and 10 T, respectively.

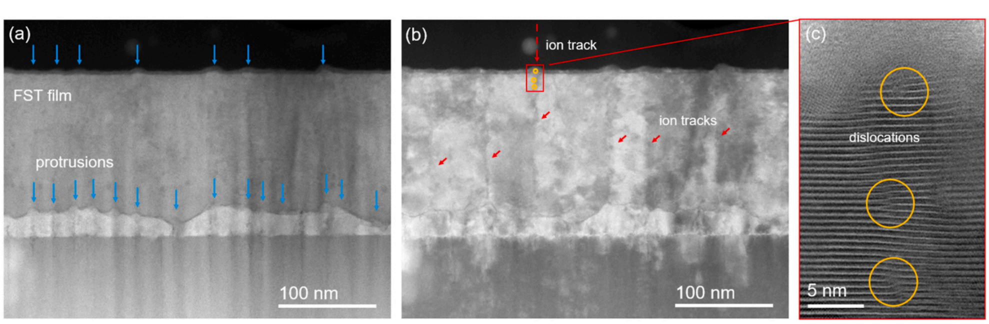

Fig. 4. (a) Z-contrast STEM image of the irradiated region showing surface and interfacial protrusions (cyan arrows) likely induced by ion impact. (b) MAADF image showing vertical defect tracks (red arrows) propagating from the surface into the film along a zigzag-like path centered on the average ion trajectory. (c) High-resolution Z-contrast view of one defect track, with dislocations (yellow circles) outlining the non-linear path while maintaining crystalline integrity.

improve compared to those of the as-grown strip. At $T = 8$ K, after the second irradiation, i.e. at $B_\phi = 10$ T, J_c (0) is 1.2×10^5 A/cm^2, already higher than the corresponding value of the as-grown strip, 9.1×10^4 A/cm^2. Below this temperature, there is an appreciable improvement even after the first irradiation. Comparable self-field J_c enhancements were found in $FeSe_{0.5}Te_{0.5}$ films grown on CeO_2 buffered $SrTiO_3$ substrate and irradiated with 190 keV protons [44]. Likewise, an increase of self-field J_c values after heavy-ion irradiation has recently been reported in YBCO thin films grown on CeO_2-buffered $SrTiO_3$ substrates and irradiated with Au ions [45] [46]. In all the studies, this phenomenon was attributed to the introduction of effective strong pinning centers, which inhibit vortex motion [47]. In fact, even in the absence of external magnetic field, the transport current flowing through the superconductor generates a magnetic field. When this self-field becomes sufficiently large, vortices begin to penetrate the film. However, the introduction in the material of correlated, even though discontinuous defects, as in our investigation, can trap the very first vortices, thereby improving the self-field J_c [45]. Remarkably, in all the investigations the self-field J_c enhancement was measured on films grown on a buffered substrate. Indeed, in the case of superconducting films, irradiation-caused damage in the substrate could induce further strain in the film with a detrimental effect on its superconducting properties [41]. The buffer layer between the substrate and the superconducting film acting as a strain absorber could mitigate this substrate-feedback effect.

At the highest temperature, 10 K, the J_c self-field value of the as-grown strip (4.9×10^4 A/cm^2) is greater than the corresponding value of the irradiated strip, both after the first and the second irradiation (respectively 2.0×10^4 A/cm^2 and 3.1×10^4 A/cm^2). This could be attributed to the difference in the superconducting critical temperatures: 15.1 K for the as-grown strip, and approximately 14.7 K and 14.4 K for the irradiated strip after the first and second irradiation processes, respectively - here T_c was determined as the temperature at which the resistivity is 10% of the normal state resistivity at the transition temperature (see Supplemental materials, Fig. S3).

However, the most noticeable effect of the irradiation processes is the marked enhancement of the in-field J_c behavior: in the magnetic field ranges comparable with the fluence equivalent field values, J_c decreases slowly compared to the as-grown strip.

To quantify this effect, the ratio Γ between the J_c of the irradiated strip and the J_c of the as-grown strip, was evaluated at several temperatures as a function of the applied magnetic field and is shown in Fig. 6 for both irradiation processes. At $T = 10$ K, for both irradiation conditions, Γ varies slightly as a function of the magnetic field and is always lower than one. This can be justified by considering the reduced temperature ($t = T/T_c$), where $t^{\text{as-grown}} = 0.78$ and $t^{\text{irradiated}} = 0.85$. Therefore, for the irradiated strip, the closer proximity to T_c leads to a reduction in J_c. For $T < 10$ K, as the temperature moves away from T_c, Γ increases in both cases and, after the irradiation at $B_\phi = 10$ T, is always $\Gamma > 1$. In particular, after the first irradiation ($B_\phi = 6$T), in the low-temperature regime Γ (0) ~ 1.5 at 6 K and Γ (0) ~ 1.75 at 4.2 K. As the magnetic field increases, Γ decreases slightly up to about 4 T, then shows a more pronounced reduction up to 8 T, and finally remains almost constant in the high-field regime, up to 18 T. In this high-field regime, Γ is approximately equal to or greater than 1. When a cumulative $B_\phi = 10$ T is reached, in the low-temperature regime, Γ (0) ~ 1.4 at 6 K and Γ (0) ~ 1.3 at 4.2 K. However, in this case, as the magnetic field increases up to about 6 T, Γ grows, reaching Γ (6 T) ~ 2 at 4.2 K, and then decreases slightly in the high-field regime. The behavior of Γ, in both irradiation cases, clearly indicates that irradiation with Au ions modifies the pinning landscape, consistent with the film's structural changes outlined in Fig. 4, by introducing a new pinning channel active in the low-temperature regime. Moreover, this effect increases by increasing the irradiation fluence.

To assess these features, we evaluated the pinning force densities ($\boldsymbol{F_p} = \boldsymbol{J_c} \times \boldsymbol{B}$) before and after irradiation in the temperature range 4.2 – 10 K, as shown in Fig. 7. At 10 K, panel d), the proximity to T_c causes the F_p of the as-grown strip to be higher than that of the irradiated strip over the entire magnetic field range. However, already at 8 K, panel c), as the temperature moves away from T_c, a marked improvement in F_p is observed after irradiation, particularly for the highest dose corresponding to an equivalent field of 10 T. This trend becomes more pronounced as the temperature is lowered to 6 K, panel b), and, especially, to 4.2 K, where the F_p values of the irradiated strip at both the irradiation doses exceed those of the as-grown strip across the whole magnetic field range, panel a). In addition, after irradiation the peak position shifts differently as the temperature increases, pointing to a different pinning landscape as will be discussed below.

Finally, we focused our attention on the values of the α-exponent (see Supplemental materials, Fig. S4), defined in the field range where J_c exhibits a power law decay with magnetic field, $J_c \sim B^{-\alpha}$ [48]. The parameter α serves as an indicator of the vortex pinning landscape. In our case, the low-T α values of the irradiated strip are lower than the corresponding values of the as-grown strip. The combination of these behaviors once again suggests that the irradiation process with Au ions at 230 MeV introduces a c-axis correlated pinning mechanism [49], mainly active at low temperatures, into the Fe(Se,Te) film. The main quantitative results are summarized in Table 1.

To deeply investigate this issue, the normalized pinning force $f_p = F_p/F_{p.max}$ (being $F_{p.max}$ the maximum value of the F_p) were analyzed in the framework of Dew-Hughes' model [50]. According to this model, f_p is expected to be proportional to $h^p(1-h)^q$ where $h = H/H_{irr}$ and p and q are constant parameter depending on the

Kind of pinning centers. Based on STEM analysis, a pinning landscape dominated by point and planar defects is expected. In the former case, the normalized pinning force is expected to scale as

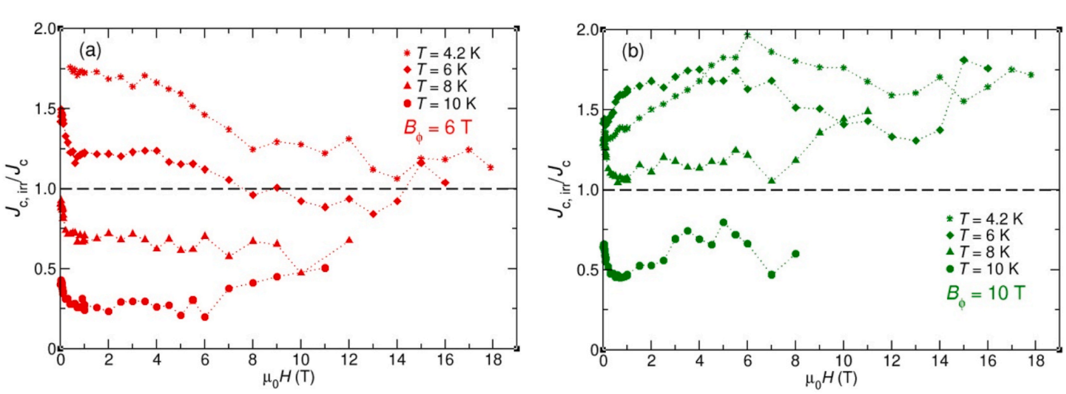

Fig. 6. (a) Ratio of the J_c of the irradiated strip (fluence-equivalent field of 6 T), to that of the as-grown strip. (b) Ratio of the J_c of the irradiated strip (cumulative fluence-equivalent field of 10 T) to that of the as-grown strip. In both cases the ratios were evaluated at T = 4.2, 6, 8, and 10 K.

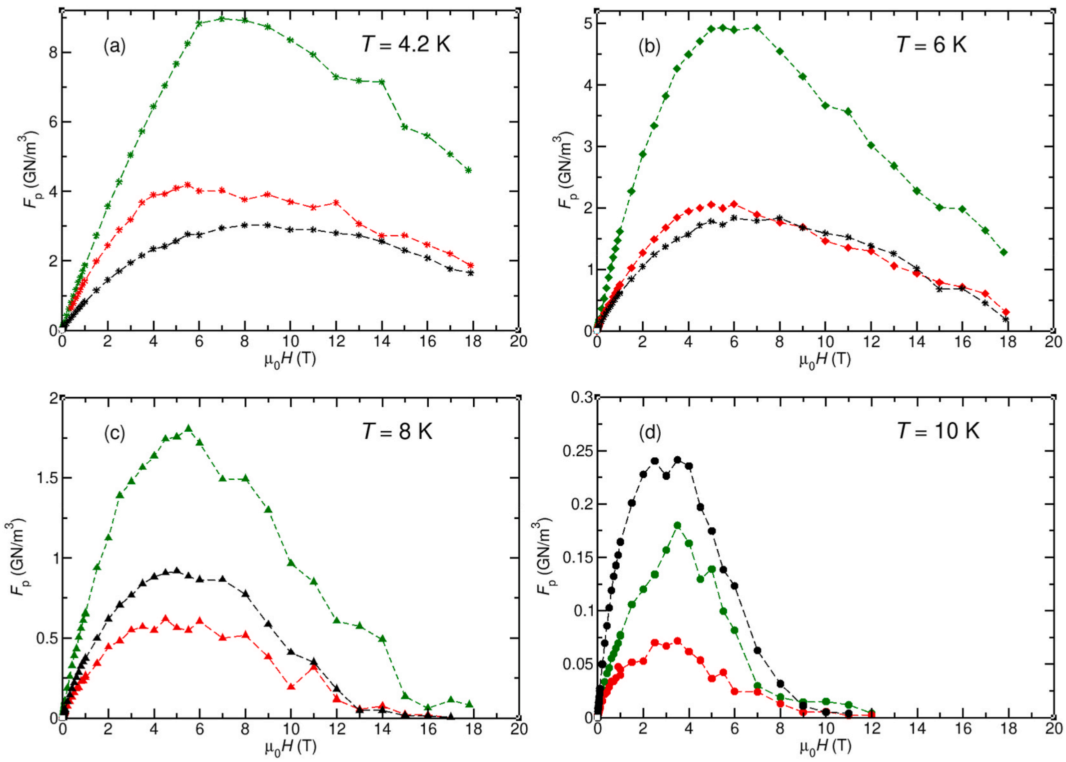

Fig. 7. Pinning force densities as a function of the applied magnetic field: (a) at 10 K, (b) at 8 K, (c) at 6 K, and (d) at 4.2 K. As adopted in Fig. 5, different colors refer to different strips: the as-grown strip data are plotted in black, the red curves refer to the irradiated strip at the dose equivalent fields $B_\phi = 6$ T and the green curves refer to the irradiated strip at the dose equivalent fields $B_\phi = 10$ T.

Table 1

Values of the pinning force maximum $\left(F_p^{Max}\right)$ and of the applied field at which it occurs ($\mu_0 H_{Max}$), of the exponent α, of the fitting parameters, p and q, in equation (3) and of the reduced magnetic field, h_p, for which the pinning force reaches its maximum ($h_{p,sp}$: from experimental data, $h_{p,fit}$: from the fit curve). The values are reported at all the investigated temperatures for the as-grown and irradiated strips.

T (K)	Sample	F_p^{Max} (GN/m^3)	$\mu_0 H_{Max}$ (T)	α	p	q	$h_{p,sp}$	$h_{p,fit}$
4.2	as- grown	4.9	9.0	0.16	0.90	1.91	0.32	0.32
	$B_\phi = 6$ T	6.8	5.5	0.13	0.82	2.41	0.19	0.25
	$B_\phi = 10$ T	9.0	7.0	0.07	1.15	3.20	0.22	0.26
6.0	as- grown	3.0	8.0	0.20	0.85	1.85	0.33	0.32
	$B_\phi = 6$ T	3.4	6.0	0.17	0.90	2.70	0.23	0.25
	$B_\phi = 10$ T	4.9	6.0	0.09	0.97	2.87	0.24	0.25
8.0	as- grown	1.5	5.0	0.22	0.94	1.87	0.33	0.33
	$B_\phi = 6$ T	1.0	4.5	0.24	0.87	1.83	0.33	0.32
	$B_\phi = 10$ T	1.8	5.5	0.22	0.93	2.00	0.33	0.32
10.0	as- grown	0.4	3.5	0.33	0.85	1.98	0.32	0.30
	$B_\phi = 6$ T	0.1	3.5	0.46	0.89	2.21	0.32	0.29
	$B_\phi = 10$ T	0.3	3.5	0.32	1.33	2.56	0.37	0.34

$$f_p(h) \propto h \cdot (1-h)^2 \quad (1)$$

implying a linear drop of the curve $J_c^{1/2}$ vs. $\mu_0 H$ at high magnetic fields and the irreversibility field $\mu_0 H_{irr}$ can be evaluated by linearly extrapolating this curve down to zero [51]. On the other hand, if the pinning is dominated by normal surface defects the normalized pinning force is expected to scale as

$$f_p(h) \propto h^{0.5} \cdot (1-h)^2 \quad (2)$$

And the Kramer's plot [52] $J_c^{1/2}(\mu_0 H)^{1/4}$ vs. $\mu_0 H$ shows a linear behaviour at high field and its extrapolation to zero can be used to determine H_{irr}. Therefore, the high-field branch of both the $J_c^{1/2}$ vs. $\mu_0 H$ and $J_c^{1/2}(\mu_0 H)^{1/4}$ vs. $\mu_0 H$ curves measured at different temperatures before and after irradiation were linearly interpolated. Then, comparing the linear correlation coefficient, r^2, case by case, we selected the more appropriate method for determining H_{irr}.

Noteworthy, for the non-irradiated strip the $J_c^{1/2}$ vs. $\mu_0 H$ curves always show a better linear trend at high field, while after irradiation the Kramer's approach works better at low temperatures. By way of example, in Fig. 8 the curves obtained at $T = 6$ K are compared. On the contrary, approaching T_c, the $J_c^{1/2}$ vs. $\mu_0 H$ curves provide higher linear correlation index also after irradiation. However, no extrapolation was required at $T = 8$ and 10 K because $\mu_0 H_{irr}$ was directly determined from the experimental data.

After establishing H_{irr} and $F_{p.max}$, the f_p vs. h curves were plotted (Fig. 9) and fitted by the equation

$$f_p(h) = \frac{(p+q)^{(p+q)}}{p^p \cdot q^q} \cdot h^p \cdot (1-h)^q \quad (3)$$

being p and q the fitting parameters, whose values are summarized in

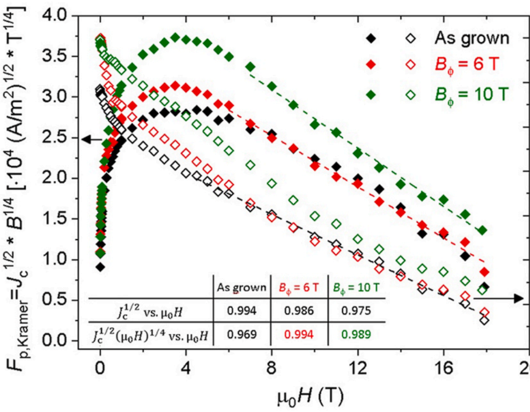

Fig. 8. Kramer's plots ($J_c^{1/2}$ $(\mu_0H)^{1/4}$, left axis, solid symbols) and $J_c^{1/2}$ plots (right axis, open symbols) as a function of μ_0H at T = 6 K for the as-grown and irradiated strips. Dashed lines are the linear fit curves providing the higher r^2 coefficient for each strip. The r^2 coefficients are summarized in the enclosed table.

Table 1. It is worth noticing that since the experimental data are a bit scattered (especially at high temperatures), the value of $F_{p.max}$ was in turn determined by fitting the experimental data F_p vs μ_0H in Fig. 7 with a polynomial equation. Fig. 9(a) and (b) evidence that, at low temperatures, the introduction of irradiation defects causes the F_p peak to move towards lower reduced field values. According to Dew-Hughes' model, the shift of the peak position from 0.32 to 0.33 to 0.19-0.26 indicates the transition from a mechanism dominated by core interaction between the flux lines and normal point-like defects to a normal surface core-pinning mechanism. Remarkably, the former mechanism is consistent with the point defect distribution evidenced by MAADF – STEM imaging, which could be caused by an inhomogeneous distribution of Se and Te [53] [54]. On the other hand, the occurrence of dislocation arrays along the ion path in the irradiated samples, which are expected to behave as normal surface defects [55] [56], support the f_p peak shift toward lower h values.

According to J_c ratio output depicted in Fig. 6, at 8 K, a slight increase of pinning force only occurs after the irradiation at the higher fluence, while irradiation at the lower fluence induced a worsening. Concurrently, the position of the f_p peak as well as p and q values are approximately the same for all the curves (Fig. 9(c) and Table 1) suggesting the predominance of a normal point pinning mechanism both before and after irradiation. The combination of these two outcomes could imply a reduced pinning efficiency of the irradiation-induced defects for temperatures higher than $T_c/2$. Further approaching the transition temperature, the sharp decrease of the pinning force after irradiation already evidenced in Fig. 7 is accompanied by the f_p peak deformation and shift towards higher reduced fields (Fig. 9(d)). The different behavior observed in the irradiated strip supports the hypothesis that irradiation-induced defects play a less important role as the temperature increases. Furthermore, the shift of the f_p peak towards values higher than 0.33 also suggests an additional contribution of Δκ-pinning (or δT_c pinning) as can be expected considering the proximity to the transition temperature [57].

The change of the pinning mechanisms with temperature in each sample is visually summed up in Fig. 10, where the f_p vs. h curves measured at various temperatures are compared for the pristine (a) and irradiated strips (b and c).

As a final analysis, in Fig. 11 we compare the angular dependence of the critical current density of the as-grown strip with that of the irradiated one. The critical current densities were evaluated as a function of

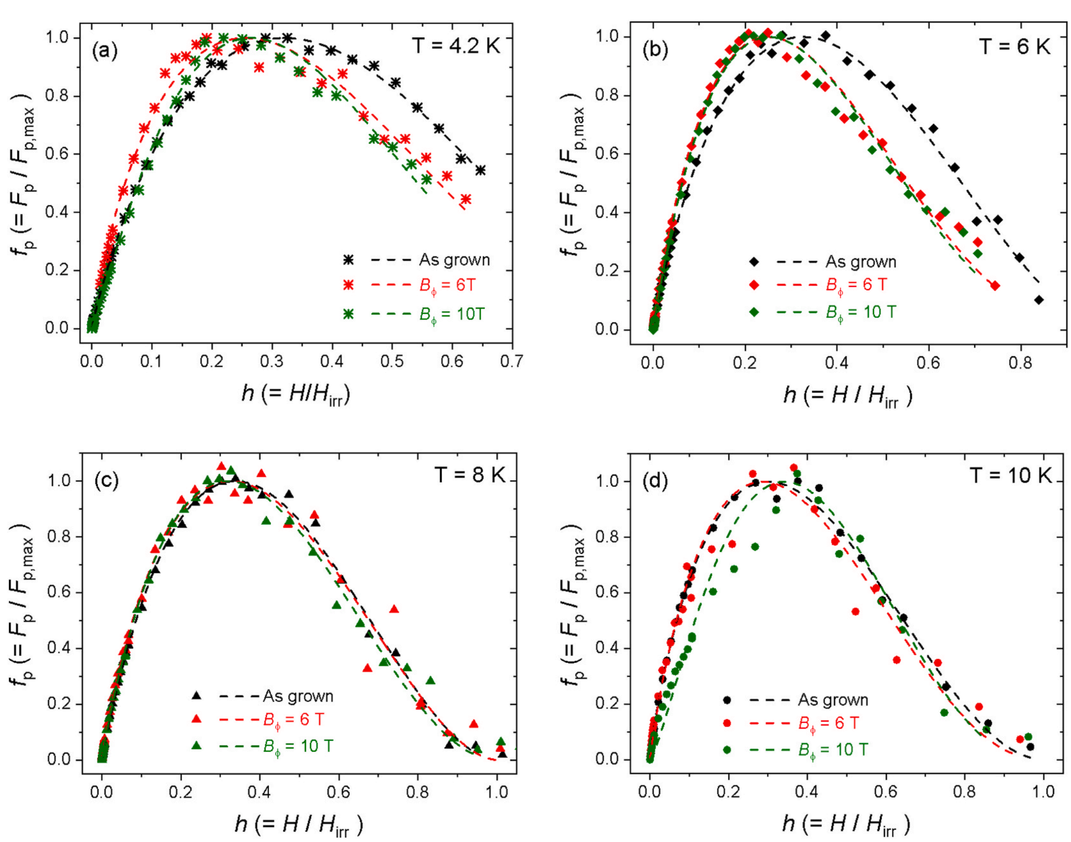

Fig. 9. Normalized flux pinning $f_p = F_p/F_{p.max}$ as a function of the reduced field $h = H/H_{irr}$ at T = 4.2 K (a), 6 K (b), 8 K (c) an 10 K (d) for the as-grown and irradiated strips. Solid lines represent the fit curves with equation (3) (see main text). The fit parameter values, p and q are summed up in Table 1, together with the reduced field of the peak position ($h_{p,sp}$: from experimental data, $h_{p,fit}$: from the fit curve).

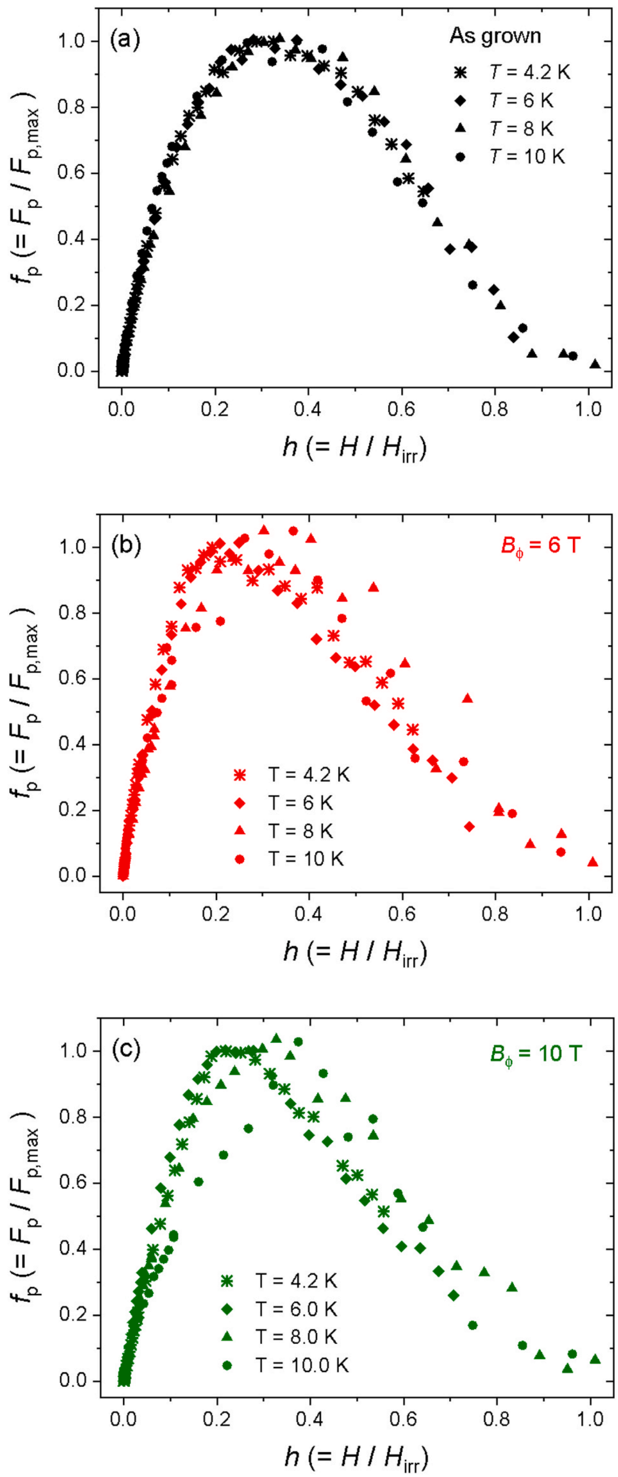

Fig. 10. Reduced field dependence of the normalized flux pinning force at various temperatures for the as grown strip (a) and for the irradiated strip at $B_\phi = 6$ T (b) and $B_\phi = 10$ T (c).

the angle between the applied magnetic field and the film surface, with 0° corresponding to the field direction parallel to the film's c-axis, i.e, to the ion irradiation direction.

It is well known that Fe(Se,Te) films exhibit low angular anisotropy, especially when compared to REBCO superconductors [58]. However, the correlated pinning landscape shown in Fig. 4 should, in principle, act beneficially to further reduce the angular anisotropy of the critical current density.

Panels (a) and (b) of Fig. 11 compare the $J_c(\theta)$ before and after both the irradiation processes evaluated at 8 K and a magnetic field magnitude of 1 T and 5 T, respectively. At the low field intensity of 1 T, panel (a), the pinning landscape introduced by the Au ion irradiation does not appear to be effective in reducing the angular anisotropy with respect to the as-grown Fe(Se,Te) film. However, as the magnitude of the applied magnetic field is increased to 5 T, panel (b), the angular dependence of the critical current in the irradiated strip becomes more isotropic. In particular, after the irradiation at the highest ion fluence, $B_\phi = 10$ T, J_c shows an almost constant behavior over the angular range from approximately −45° to 45°.

To quantify this effect, we evaluated the angular anisotropy parameter, defined as $\gamma_\theta = J_c\,(H//a,b)/J_c\,(H//c)$, as reported in Table 2. At a temperature of 8 K and magnetic field of 1 T, $\gamma_\theta^{\text{as-grown}} = 1.23$, which is lower than the parameters observed for the irradiated samples: $\gamma_\theta^{6T} = 1.59$ and $\gamma_\theta^{10T} = 1.39$. However, when the magnetic field is increased to 5 T, $\gamma_\theta^{6T} = 1.56$ becomes comparable to $\gamma_\theta^{\text{as-grown}} = 1.59$, while $\gamma_\theta^{10T} = 1.25$ decreases further, suggesting that the correlated pinning landscape described in Fig. 4 becomes active. As the temperature decreases, the effectiveness of the correlated pinning contribution becomes more evident. At 6 K and 5 T, panel (c), after the irradiation at $B_\phi = 10$ T J_c is not only nearly constant over the whole angular range but also exhibits a moderate bump around 0. This confirms the effectiveness of this correlated pinning landscape induced by irradiation. When the magnetic field is enhanced at 7 T, panel (d), the bump disappears. However, the angular dependence of the critical current density remains almost unchanged. Conversely, the J_c vs θ curves measured before and after the first irradiation at the fluence-equivalent field of 6 T collapse on each other at both magnetic field magnitudes.

Finally, as reported in Table 2, at 4.2 K the relation $\gamma_\theta^{\text{as-grown}} > \gamma_\theta^{6T} > \gamma_\theta^{10T}$ is observed at both applied magnetic fields, 5 T and 7 T. In addition, the angular dependence of the critical current density after both the irradiation processes exhibits lower anisotropy compared to the as-grown strip across the entire range, as shown in panels (e) and (f) of Fig. 11. In agreement with the previous discussions, this behavior suggests that the Au ion irradiation has introduced a new correlated pinning channel that is active in the low-temperature and up to mid-to-high field regime.

4. Conclusions

In this paper we thoroughly investigated the effect of 230 MeV Au-ion irradiation on the pinning properties of Fe(Se,Te) films grown on CZO buffered YSZ substrates, and correlated the observations from a comprehensive analysis of structural features performed through STEM with the analysis of transport properties such as critical current density and pinning force as a function of temperature as well as magnitude and orientation of the applied field.

STEM imaging revealed surface and interfacial protrusions which can be attributed to ion impact especially at interfaces, and vertically extended defect tracks from the surface through the whole superconducting film thickness, which are composed of dislocation chains. The overall defect configuration introduced by the ion irradiation consisted of vertical dislocation arrays, which can be interpreted as planar defects tracing the path of the ion through the film and interacting with the pre-existing pinning landscape modifying its strength and anisotropy.

The most noticeable effect of the irradiation processes on the transport properties is the marked enhancement of J_c: in the magnetic field ranges comparable with the fluence equivalent field values, J_c decreases slowly compared to the as-grown strip. After both the irradiations, the analysis of the behavior of the ratio between J_c of the irradiated strip and J_c of the as-grown one clearly indicated that Au-ions irradiation modifies the pinning landscape, by introducing a new pinning channel more active in the low-temperature regime and more effective as the irradiation fluence increases. These results are consistent with the observation

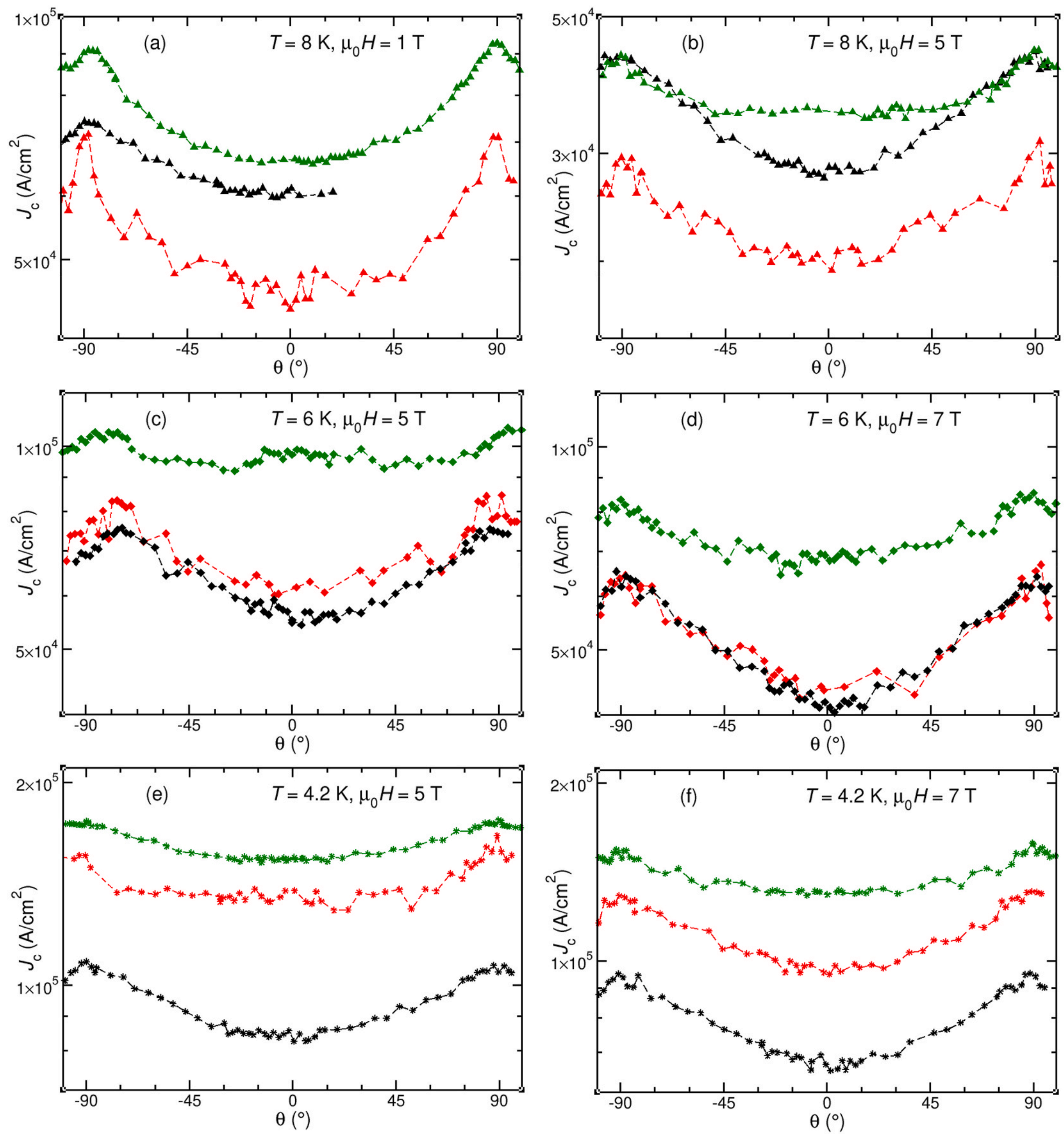

Fig. 11. Angular behavior of the critical current density, at different temperature and applied magnetic field values, for the as grown strip (black curves) and the irradiated strip, after each irradiation process (fluence-equivalent field $B_\phi = 6$ T (red curves), fluence-equivalent field $B_\phi = 10$ T (green curves)).

Table 2
Values of the angular anisotropy parameter γ_θ evaluated at $\mu_0H = 1$ T, 5 T and 7 T. The values are reported for the as-grown and irradiated strips at all at all the investigated temperatures for the as-grown and irradiated strips.

T (K)	Sample	γ_θ^{1T}	γ_θ^{5T}	$\gamma_\theta^{7\,T}$
4.2	as- grown	-	1.25	1.45
	$B_\phi = 6$ T	-	1.20	1.37
	$B_\phi = 10$ T	-	1.12	1.22
6.0	as- grown	-	1.39	1.64
	$B_\phi = 6$ T	-	1.37	1.54
	$B_\phi = 10$ T	-	1.08	1.25
8.0	as- grown	1.23	1.59	-
	$B_\phi = 6$ T	1.59	1.56	-
	$B_\phi = 10$ T	1.39	1.25	-

of a c-axis correlated pinning mechanism active at low temperature emerging from the analysis of the pinning forces vs field and temperature. The effectiveness of this new correlated pinning channel is also confirmed by the angular dependence of the critical current density, which after both the irradiation processes exhibits an increase of the ratio between J_c ($H//c$) and J_c ($H//a,b$) compared to the as-grown strip values, namely a lower J_c anisotropy across the entire range of investigated fields.

All these results confirm that irradiation is a very powerful tool for tailoring the electromagnetic properties of Fe(Se,Te) superconducting films in a controlled way, thereby enabling their functionalization for targeted applications.

CRediT authorship contribution statement

Francesco Rizzo: Conceptualization, Data curation, Formal analysis, Investigation, Supervision, Visualization, Writing – original draft, Writing – review & editing. **Mario Scuderi:** Conceptualization, Data curation, Formal analysis, Funding acquisition, Investigation, Supervision, Visualization, Writing – original draft, Writing – review & editing. **Valeria Braccini:** Conceptualization, Data curation, Formal analysis, Resources, Supervision, Visualization, Writing – original draft, Writing – review & editing. **Emilio Bellingeri:** Resources. **Michela Iebole:** Resources. **Alberto Martinelli:** Resources. **Nicola Manca:** Resources. **Matteo Cialone:** Resources. **Marina Putti:** Conceptualization, Funding acquisition. **Andrea Augieri:** Investigation. **Laura Piperno:** Resources. **Angelo Vannozzi:** Writing – review & editing. **Maria Laura Amoruso:**

Data curation, Visualization. **Fortunato Neri:** Funding acquisition. **Michela Fracasso:** Formal analysis, Writing – review & editing. **Roberto Gerbaldo:** Funding acquisition, Resources. **Gianluca Ghigo:** Conceptualization, Writing – review & editing. **Daniele Torsello:** Conceptualization, Resources, Writing – review & editing. **Laura Gozzelino:** Conceptualization, Data curation, Formal analysis, Software, Supervision, Visualization, Writing – original draft, Writing – review & editing.

Declaration of competing interest

The authors declare that they have no known competing financial interests or personal relationships that could have appeared to influence the work reported in this paper.

Acknowledgements

We acknowledge the partial financial support from MUR funded PRIN project HIBiSCUS 201785KWLE, from the Joint Research Agreement Eni-CNR, from INFN-CSN5 under the experiment SuperMAD, from the project Space It Up funded by the Italian Space Agency, ASI, and the Ministry of University and Research, MUR, under Contract No. 2024-5-E.0 - CUP n. I53D24000060005, and from the project NODES, which has received funding from the MUR - M4C2 1.5 of PNRR funded by the European Union – NextGenerationEU (Grant agreement no. ECS00000036).

TEM characterization was carried out using the facilities provided by the Italian Infrastructure Beyond-Nano UPGRADE – Materials and processes Beyond the Nano-scale (CUP: DFM.AD006.173 .. funded by CNR-Dipartimento Scienze Fisiche e Tecnologie della Materia.

We are grateful to the staff of INFN-LNL for their assistance during irradiation experiments and to F. Laviano for fruitful and stimulating discussions.

Appendix A. Supplementary data

Supplementary data to this article can be found online at https://doi.org/10.1016/j.supcon.2026.100262.

References

[1] Hosono H, Tanabe K, Takayama-Muromachi E, Kageyama H, Yamanaka S, Kumakura H, Nohara M, Hiramatsu H, Fujitsu S. Exploration of new superconductors and functional materials, and fabrication of superconducting tapes and wires of iron pnictides. Sci Technol Adv Mater 2015;16(3):33503. https://doi.org/10.1088/1468-6996/16/3/033503.

[2] Iida K. Status of iron based superconductors: characteristics and relevant properties for applications. IEEE Trans Appl Supercond 2025;35(5):7400109. https://doi.org/10.1109/TASC.2025.353091.

[3] Liu L, Ye J, Mou S, Zhu R, Miao C, Li Y, Shi Z, Qi Y, Ge J, Liu H, Liu F, Zhang Z. Fabrication of meter-long class Fe(Se,Te)-coated conductors with high superconducting performance. Adv Eng Mater 2023;25:2201536. https://doi.org/10.1002/adem.202201536.

[4] Dong C, Xu Q, Ma Y. Towards high-field applications: high-performance, low-cost iron-based superconductors. Natl Sci Rev 2024;11(11):nwae122. https://doi.org/10.1093/nsr/nwae122.

[5] Zhao J, Liao J, Dong C, Wang D, Ma. Properties and applications of iron–chalcogenide superconductors. Materials 2024;17:3059. https://doi.org/10.1002/adem.202201536.

[6] Iida K, Yamauchi Y, Hatano T, et al. Structural analysis and transport properties of [010]-tilt grain boundaries in Fe(Se,Te). Sci Technol Adv Mater 2024;25(1):2384829. https://doi.org/10.1080/14686996.2024.2384829.

[7] Iida K. Grain boundary characteristics of Fe-based superconductors. Supercond Sci Technol 2020;33(4):43001. https://doi.org/10.1088/1361-6668/ab73ef.

[8] Gurevich A. Iron-based superconductors at high magnetic fields. Rep Prog Phys 2011;74:124501. https://doi.org/10.1088/0034-4885/74/12/124501.

[9] Pyon S, Ito T, Sasaki T, et al. Record-high critical current density in $(Ba,Na)Fe_2As_2$ round wire suitable for high-field applications. Phys C: Supercond Appl 2023;615:1354354. https://doi.org/10.1016/j.physc.2023.1354354.

[10] Traverso A, Bordonaro M, Ul Hassan HM, et al. Impact of powder granulometry on the transport properties of $Ba_{0.6}K_{0.4}Fe_2As_2$ superconducting tapes. IEEE Trans Appl Supercond 2025;35(5):7300405. https://doi.org/10.1109/TASC.2025.3534744.

[11] Zhang X, Ma Y. Progress in the development of the 122-type IBS wires. Superconductivity 2022;2:100010. https://doi.org/10.1016/j.supcon.2022.100010.

[12] Zhang X, Oguro H, Yao C, et al. Superconducting properties of 100-m class Sr0:6K0:4Fe2As2 tape and pancake coils. IEEE Trans Appl Supercond 2017;27:7300705. https://doi.org/10.1109/TASC.2017.2650408.

[13] Ding H, Zhao H, Huang P, et al. Development of the first Tesla class iron-based superconducting coil for high field application. Supercond Sci Technol 2023;36:11LT01. https://doi.org/10.1088/1361-6668/acfa29.

[14] Palombo M, Malagoli A, Pani M, Bernini C, Manfrinetti P, Palenzona A, Putti M. Exploring the feasibility of Fe(Se,Te) conductors by ex-situ powder-in-tube method. J Appl Phys 2015;117:213903. https://doi.org/10.1063/1.4921902.

[15] Bellingeri E, Buzio R, Gerbi A, Marrè D, Congiu S, Cimberle MR, Tropeano M, Siri AS, Palenzona A, Ferdeghini C. High quality epitaxial $FeSe_{0.5}Te_{0.5}$ thin films grown on SrTiO3 substrates by pulsed laser deposition. Supercond Sci Technol 2009;22:105007. https://doi.org/10.1088/0953-2048/22/10/105007.

[16] Braccini V, Kawale S, Reich E, Bellingeri E, Pellegrino L, Sala A, Putti M, Higashikawa K, Kiss T, Holzapfel B, Ferdeghini C. Highly effective and isotropic pinning in epitaxial Fe(Se,Te) thin films grown on CaF_2 substrates. Appl Phys Lett 2013;103:172601. https://doi.org/10.1063/1.4826677.

[17] Seo S, Noh H, Li N, et al. Artificially engineered nanostrain in $FeSe_xTe_{1-x}$ superconductor thin films for supercurrent enhancement. NPG Asia Mater 2020;12:7. https://doi.org/10.1038/s41427-019-0186-y.

[18] Mele P. Superconducting properties of iron chalcogenide thin films. Sci Technol Adv Mater 2012;13(5):54301. https://doi.org/10.1088/1468-6996/13/5/054301.

[19] Si W, Han SJ, Shi X, Ehrlich SN, Jaroszynski J, Goyal A, Li Q. High current superconductivity in $FeSe_{0.5}Te_{0.5}$-coated conductors at 30 tesla. Nat Commun 2013;4:1347. https://doi.org/10.1038/ncomms2337.

[20] Piperno L, Vannozzi A, Augieri A, Masi A, Mancini A, Rufoloni A, Celentano G, Braccini V, Cialone M, Iebole M, Manca N, Martinelli A, Meinero M, Putti M, Meledin A. High-performance Fe(Se,Te) films on chemical CeO_2-based buffer layers. Sci Rep 2023;13(1):569. https://doi.org/10.1038/s41598-022-24044-5.

[21] Song J, Xu Z, Xiong X, et al. Critical role played by interface engineering in weakening thickness dependence of superconducting and structural properties of FeSe0.5Te0.5-Coated conductors. ACS Appl Mater Interfaces 2023;15:26215. https://doi.org/10.1021/acsami.3c04531.

[22] Mou S, Ye J, Zhu R, et al. Effect of the buffer layers on the performance of Fe(Se,Te) films fabricated on IBAD metal templates by pulsed laser deposition. J Supercond Nov Magnetism 2023;36:793–802. https://doi.org/10.1007/s10948-023-06504-9.

[23] Zhou X, Li W, Hou Q, Wei W, Liu W, Wang Ke, Xing X, Liu L, Ge J, Qi Y, Liu H, Ren L, Tamegai T, Sun Y, Shi X. Critical current density and AC magnetic susceptibility of high-quality $FeTe_{0.5}Se_{0.5}$ superconducting tapes. Superconductivity 2024;12:100127. https://doi.org/10.1016/j.supcon.2024.100127.

[24] Thomas AA, Shipulin IA, Holleis S, Eisterer M, Nielsch K, Huhne R. Comparative study of Fe(Se,Te) thin films on flexible coated conductor templates and single-crystal substrates. Supercond Sci Technol 2021;34:115013. https://doi.org/10.1088/1361-6668/ac2557.

[25] Wie S, Liu X, Zhang Z, et al. First performance test of $FeSe_{0.5}Te_{0.5}$-coated conductor coil under high magnetic fields. Supercond Sci Technol 2023;36. https://doi.org/10.1088/1361-6668/acba4d. 04LT01.

[26] Holleis S, Thomas AA, Shipulin IA, Hühne R, Steiger-Thirsfeld A, Bernardi J, Eisterer M. Magnetic granularity in PLD-grown Fe(Se,Te) films on simple RABiTS templates. Supercond Sci Technol 2022;35:74001. https://doi.org/10.1088/1361-6668/ac6cab.

[27] Sylva G, Augieri A, Mancini A, Vannozzi A, Celentano G, Bellingeri E, Ferdeghini C, Putti M, Braccini V. Fe(Se,Te) coated conductors deposited on simple rolling assisted biaxially textured substrate templates. Supercond Sci Technol 2019;32:84006. https://doi.org/10.1088/1361-6668/ab0e98.

[28] Sylva G, Bellingeri E, Bernini C, et al. The role of texturing and thickness of oxide buffer layers in the superconducting properties of Fe(Se,Te) coated conductors. Supercond Sci Technol 2020;33:114002. https://doi.org/10.1088/1361-6668/abb35d.

[29] Mancini A, Masi A, Sung Z, Taheri B, Vannozzi A, Angrisani Armenio A, Rufoloni A, Piperno L, Celentano G. Titanium nitride epitaxial film: innovative non-oxide buffer layer for Fe(Se,Te) coated conductors. IEEE Trans Appl Supercond 2025;35:6601105. https://doi.org/10.1109/TASC.2024.3516735.

[30] Piperno L, Vannozzi A, Pinto V, et al. Chemical CeO_2-based buffer layers for Fe(Se,Te) films. IEEE Trans Appl Supercond 2022;32(4):7300205. https://doi.org/10.1109/TASC.2022.3142709.

[31] Piperno L, Vannozzi A, Rizzo F, et al. Low-cost architecture for iron-based coated conductors. iScience 2024;27:111032. https://doi.org/10.1016/j.isci.2024.111032.

[32] Torsello D, Gozzelino L, Gerbaldo R, Tamegai T, Ghigo G. Scaling laws for ion irradiation effects in iron-based superconductors. Sci Rep 2021;11:5818. https://doi.org/10.1038/s41598-021-84699-4.

[33] Civale L. Properties and applications of iron–chalcogenide superconductors. Materials 2024;17:3059. https://doi.org/10.1002/adem.202201536.

[34] Lang M, Djurabekova F, Medvedev N, Toulemonde M, Trautmann C. Fundamental phenomena and applications of swift heavy ion irradiations. In: Konings Rudy JM, Stoller Roger E, editors. Comprehensive nuclear materials. second ed. Elsevier; 2020. p. 485–516. https://doi.org/10.1016/B978-0-12-803581-8.11644-3.

[35] Torsello D, Gerbaldo R, Gozzelino L, Laviano F, Takahashi A, Park A, Pyon S, Ichinose A, Tamegai T, Ghigo G. Twofold role of columnar defects in iron based superconductors. Supercond Sci Technol 2020;33:94012. https://doi.org/10.1088/1361-6668/aba350.

[36] Fracasso M, Scuderi M, Brugaletta E, et al. Effects of high-energy Pb-ion irradiation on critical current and flux pinning in Fe(Se,Te) thin films. Supercond Sci Technol 2025;38(10):105021. https://doi.org/10.1088/1361-6668/ae0fc6.
[37] Massee F, Sprau PO, Wang Y-L, Séamus Davis JC, Ghigo G, Gu G, Kwok W-K. Imaging atomic-scale effects of high-energy ion irradiation on superconductivity and vortex pinning in Fe(Se,Te). Sci Adv 2015;1(4):e1500033. https://doi.org/10.1126/sciadv.1500033.
[38] Tamegai T, Taen T, Yagyuda H, et al. Effects of particle irradiations on vortex states in iron-based superconductors. Supercond Sci Technol 2012;25(8):84008. https://doi.org/10.1088/0953-2048/25/8/084008.
[39] Vannozzi A, Piperno L, Rufoloni A, et al. Zr:CeO_2 buffer by CSD on Ni-W substrate for low-cost Fe(Se,Te) coated conductor. IEEE Trans Appl Supercond 2024;34(3):7500305. https://doi.org/10.1109/TASC.2024.3354220.
[40] Palenzona A, Sala A, Bernini C, Braccini V, Cimberle MR, Ferdeghini C, Lamura G, Martinelli A, Pallecchi I, Romano G. A new approach for improving global critical current density in Fe($Se_{0.5}Te_{0.5}$) polycrystalline materials. Supercond Sci Technol 2012;25(11):115018. https://doi.org/10.1088/0953-2048/25/11/115018.
[41] Sylva G, Bellingeri E, Ferdeghini C, Martinelli A, Pallecchi I, Pellegrino L, Putti M, Ghigo G, Gozzelino L, Torsello D, Grimaldi G, Leo A, Nigro A, Braccini V. Effects of high-energy proton irradiation on the superconducting properties of Fe(Se,Te) thin films. Supercond Sci Technol 2018;31(5):54001. https://doi.org/10.1088/1361-6668/aab3bd.
[42] Ziegler JF, Ziegler MD, Biersack JP. SRIM – the stopping and range of ions in matter. Nucl Instrum Methods Phys Res B 2020;268:1818–23. https://doi.org/10.1016/j.nimb.2010.02.091.
[43] Vannozzi A, Prili S, Sylva G, et al. Epitaxial Zr-doped CeO2 films by chemical solution deposition as buffer layers for Fe (Se, Te) film growth. Supercond Sci Technol 2020;33(8):84004. https://doi.org/10.1088/1361-6668/ab9aa7.
[44] Ozaki T, Wu L, Zhang C, Jaroszynski J, Si W, Zhou J, Zhu Y, Li Q. A route for a strong increase of critical current in nanostrained iron-based superconductors. Nat Commun 2016;7:13036. https://doi.org/10.1038/ncomms13036.
[45] Matsui H, Yamaguchi I. Enhancement of self-field critical current density by several-tens-MeV ion irradiation in $YBa_2Cu_3O_7$ films prepared by fluorine-free metal-organic deposition. Jap J Appl Phys 2022;61:43001. https://doi.org/10.35848/1347-4065/ac5265.
[46] Matsui H, Yamaguchi I, Ishikawa N. Systematic enhancement of self-field critical current density in $YBa_2Cu_3O_7$ films by heavy-ion irradiation. Phys Scripta 2025;100:75917. https://doi.org/10.1088/1402-4896/adde93.
[47] Talantsev EF, Tallon JL. Universal self-field critical current for thin-film superconductors. Nat Commun 2016;6:7820. https://doi.org/10.1038/ncomms8820.
[48] Dam B, Huijbregtse JM, Klaassen FC, et al. Origin of high critical currents in $YBa_2Cu_3O_{7-\delta}$ superconducting thin films. Nature 1999;399:439. https://doi.org/10.1038/20880.
[49] Rizzo F, Augieri A, Kursumovic A, et al. Pushing the limits of applicability of REBCO coated conductor films through fine chemical tuning and nanoengineering of inclusions. Nanoscale 2018;10:8187–95. https://doi.org/10.1039/C7NR09428K.
[50] Dew-Hughes D. Flux pinning mechanisms in type II superconductors. Philos Mag 1974;30(2):293–305. https://doi.org/10.1080/14786439808206556.
[51] Li M, Chen L, You WL, Ge J, Zhang J. Giant increase of critical current density and vortex pinning in Mn doped $K_xFe_{2-y}Se_2$ single crystals. Appl Phys Lett 2014;105(19):192602. https://doi.org/10.1063/1.4901902.
[52] Kramer EJ. Scaling laws for flux pinning in hard superconductors. J Appl Phys 1973;44(3):1360–70. https://doi.org/10.1063/1.1662353.
[53] Si W, Zhou J, Jie Q, Dimitrov I, Solovyov V, Johnson PD, Jaroszynski J, Matias V, Sheehan C, Li Q. Iron-chalcogenide $FeSe_{0.5}Te_{0.5}$ coated superconducting tapes for high field applications. Appl Phys Lett 2011;98(26):262509. https://doi.org/10.1063/1.3606557.
[54] Ye J, Mou S, Zhu R, Liu L, Li Y. Evolution of superconductivity dependence on substrate temperature with thickness of Fe (Se, Te) coated conductors deposited on metal tapes. J Appl Phys 2022;132(18):183910. https://doi.org/10.1063/5.0122319.
[55] Crisan A, Dang VS, Yearwood G, Mikheenko P, Huhtinen H, Paturi P. Investigation of the bulk pinning force in YBCO superconducting films with nano-engineered pinning centres. Physica C 2014;503:89–93. https://doi.org/10.1016/j.physc.2014.03.028.
[56] Mele P, Crisan A, Adam MI. Pinning-engineered $YBa_2Cu_3O_x$ thin films. In: Crisan A, editor. Vortices and nanostructured superconductors, vol. 261. Cham: Springer International Publishing; 2017. p. 15–63.
[57] Koblischka MR, Muralidhar M. Pinning force scaling analysis of Fe-based high-T_c superconductors. Int J Mod Phys B 2016;30:1630017. https://doi.org/10.1142/S0217979216300176.
[58] Grimaldi G, Khan MR, Leo A, et al. Unveiling intrinsic material and extrinsic pinning dimensionality in superconductors: why Fe(Se,Te) is able to mimic YBCO. iScience 2024;27(4):109422. https://doi.org/10.1016/j.isci.2024.109422.